

# A Restoration Framework for Ultrasonic Tissue Characterization

Martino Alessandrini, Simona Maggio, Jonathan Porée, Luca De Marchi, Nicolo Speciale, Emilie Franceschini, Olivier Bernard, and Olivier Basset

**Abstract**—Ultrasonic tissue characterization has become an area of intensive research. This procedure generally relies on the analysis of the unprocessed echo signal. Because the ultrasound echo is degraded by the non-ideal system point spread function, a deconvolution step could be employed to provide an estimate of the tissue response that could then be exploited for a more accurate characterization. In medical ultrasound, deconvolution is commonly used to increase diagnostic reliability of ultrasound images by improving their contrast and resolution. Most successful algorithms address deconvolution in a maximum *a posteriori* estimation framework; this typically leads to the solution of  $\ell^2$ -norm or  $\ell^1$ -norm constrained optimization problems, depending on the choice of the prior distribution. Although these techniques are sufficient to obtain relevant image visual quality improvements, the obtained reflectivity estimates are, however, not appropriate for classification purposes. In this context, we introduce in this paper a maximum *a posteriori* deconvolution framework expressly derived to improve tissue characterization. The algorithm overcomes limitations associated with standard techniques by using a nonstandard prior model for the tissue response. We present an evaluation of the algorithm performance using both computer simulations and tissue-mimicking phantoms. These studies reveal increased accuracy in the characterization of media with different properties. A comparison with state-of-the-art Wiener and  $\ell^1$ -norm deconvolution techniques attests to the superiority of the proposed algorithm.

## I. INTRODUCTION

MEDICAL ultrasound is widely employed in the clinical routine to assess possible abnormalities in several parts of the human body. Currently, the diagnosis relies almost exclusively on the visual observation of the ultrasound sequences, but it has been widely reported that computer analysis of the echo signal can be employed to infer diagnostically relevant information on the tissue

state which is otherwise imperceptible from simple visual inspection. This observation motivated the development of computer-aided detection (CAD) tools to function as a support to the physician in the interpretation of ultrasound scans and to guide the physician in the decision-making process in the case of suspicious situations. The use of CAD tools on clinical data has led to relevant results in several applications, such as prostate cancer detection on trans-rectal ultrasound images [1], detection of suspicious masses in breast ultrasound [2], and diagnosis of hepatic steatosis [3].

The output of CAD systems is derived from the quantitative analysis of the echo signal. In this context, a large number of features of different natures have been proposed in literature; these can be subdivided according to their contribution in highlighting specific tissue properties. Tissue characterization based on the acoustic parameters such as attenuation and backscattering coefficients extracted from RF echo signals has been widely studied. These quantities are commonly estimated by using 1-D [4] or 2-D [5] spectral analysis of the RF signal. Spectral features have proven to provide useful output for diagnosis of diseases in various organs, such as the eye, prostate, breast, and liver; see [6] for a comprehensive review. In addition to RF-spectrum analysis, many researchers have used texture features extracted from ultrasound B-scan images for characterization purposes, because the speckle pattern in the ultrasonic image can reveal structural information about the tissue. Usefulness of textural features within clinical settings has been widely documented, e.g., for prostate carcinoma diagnosis [7], [8], evaluation of liver diseases such as hepatoma and cirrhosis [9], and detection of atherosclerotic plaques in the carotid artery [10].

A third class of features derives from modeling the echo signal amplitude distribution by means of suitable parametric probability density functions (pdfs). These statistical features have been shown to be well-related to scatterer concentration and distribution pattern. A variety of models have been proposed in literature. The most popular model is represented by the Rayleigh distribution for the envelope signal, which can be analytically derived for diffusive scattering (or fully developed speckle) regions [11, pp. 48–50], [12]. Nevertheless, diffuse scattering conditions are often violated in biological tissues, either because the number of scatterers per resolution cell may not be large enough, or because of the presence of regular patterns in the scatterers location. In these cases, more complex models must be adopted, such as Rician [11, pp. 50–52], K [13], Homodyne-K [14], or Nakagami distribution [15]. In

Manuscript received October 22, 2010; accepted August 25, 2011.

M. Alessandrini is with the Advanced Research Center on Electronic Systems for Information and Communication Technologies E. De Castro (ARCES), Università di Bologna, Bologna, Italy (e-mail: martino.alessandrini@creatis.insa-lyon.fr).

S. Maggio, L. De Marchi, and N. Speciale are with the Dipartimento di Elettronica, Informatica e Sistemistica (DEIS), Università di Bologna, Bologna, Italy.

J. Porée, O. Bernard, and O. Basset are with Centre de Recherche et d'Applications en Traitement de l'Image et du Signal (CREATIS), Centre National de la Recherche Scientifique (CNRS) UMR 5220, Institut National de la Santé et de la Recherche Médicale (INSERM) U630, Université de Lyon, Institut National des Sciences Appliquées (INSA)-Lyon, Villeurbanne, France.

E. Franceschini is with the Laboratoire de Mécanique et d'Acoustique (LMA), Centre National de la Recherche Scientifique (CNRS), UPR 7051, Marseille, France.

Digital Object Identifier 10.1109/TUFFC.2011.2092

particular, from the seminal paper [15], Nakagami features used for tissue typing have been thoroughly explored [16], [17]. Although originally proposed for an uncompressed envelope, Nakagami parameters have also been shown to possess good discriminating properties on B-mode, logarithmically compressed data [18]. When the raw RF signal is considered, KRF [19] and generalized Gaussian distribution [20] are the most comprehensive models. Because of their computational feasibility and attested diagnostic relevance [16], [19], statistical features are particularly well suited for those applications in which online assistance must be provided, such as for biopsy guidance.

These features are normally computed directly on acquired echo data. Nevertheless, because of the blurring associated with the system point spread function (PSF), the backscattered echo is known to carry degraded information about the tissue, and the potential of standard CAD schemes is thus reduced. In this context, our goal is to employ a deconvolution step to restore a tissue response estimate, and then to achieve improved tissue characterization by making use of features computed on the deconvolved data.

The problem of deconvolution of medical ultrasound images has received some attention in recent years; see [21] for a review. The aim is to improve readability and diagnostic reliability of ultrasound images by removing, to the maximum extent possible, the blurring effect associated with the PSF of the acquisition system. The most common way to tackle deconvolution is as a maximum *a posteriori* (MAP) estimation problem. The corresponding mathematical formulation leads to the solution of  $\ell^2$ -norm [22], [23] or  $\ell^1$ -norm constrained optimization tasks [24]–[26], depending on the choice of the prior distribution. Although these techniques are sufficient for obtaining relevant image visual quality improvements, they are not sufficient to retrieve reflectivity estimates which would be suitable in a classification context. This is related to a statistical biasing effect which is connected to the choice of a reflectivity model that is too simple to represent a real tissue structure.

In this context, this paper<sup>1</sup> contributes to the related literature in two ways:

- The capabilities of standard deconvolution techniques are analyzed for use in a tissue characterization context. These will be theoretically derived and experimentally tested both with simulations and real acquisitions. In a previous paper [8], we employed deconvolution, implemented as a linear prediction adaptive filter, in a characterization context. Some improvements were observed in classification accuracy for prostate cancer detection. However, here we methodically study the properties of state-of-the-art

deconvolution algorithms in the considered perspective. To the best of our knowledge, a similar analysis is completely missing from the literature.

- A novel deconvolution technique is introduced to overcome the limitations associated with standard methods. Hence, the final goal is moved from enhancement of the image’s visual quality to the restoration of statistically close estimates of the tissue response. The algorithm is mathematically formulated in terms of a MAP estimation problem solved in an expectation maximization (EM) framework. A non-standard statistical model for the reflectivity is employed, represented by a generalized Gaussian distribution (GGD) [27]. The performance of the new algorithm is evaluated and compared with standard techniques.

The remainder of the paper is organized as follows. In Section II, the Bayesian framework for image deconvolution is recalled, along with the most common solutions. In Section III, the proposed deconvolution technique is presented and the key elements of novelty over existing ones are highlighted. In Section IV, the experimental setup for making the acquisitions is presented, along with the processing flowchart adopted for the performance evaluation. In Section V, results from computer simulations and real acquisitions are presented. Concluding considerations and hints on future research directions are provided in Section VI.

## II. DECONVOLUTION OF MEDICAL ULTRASOUND IMAGES

The Bayesian formulation provides an effective way to tackle the deconvolution problem as far as medical ultrasound is concerned. Because the approach has been thoroughly explored in the literature, only the basic equations are reported here; the interested reader may find more detailed derivations in, e.g., [21, ch. 5], and in the papers referred to throughout the text.

### A. Bayesian Formulation

Assuming propagation through soft tissues and using the first-order Born approximation (weak scattering), a linear model can account for the interactions between the acoustic beam and the tissue [28], [29]. The linear image formation model can be compactly expressed as

$$\mathbf{y} = \mathbf{H}\mathbf{x} + \boldsymbol{\nu}, \quad (1)$$

where  $\mathbf{y}$  is the RF echo image;  $\mathbf{x}$  is the medium response, or reflectivity; and  $\boldsymbol{\nu}$  is the measurement noise. The system matrix  $\mathbf{H}$  accounts for the 2-D convolution with the system PSF (see [30, Appendix A]). Note that all  $\mathbf{y}$ ,  $\mathbf{x}$ , and  $\boldsymbol{\nu}$  are intended to be arranged into vectors via lexicographical ordering. Deconvolution is then intended to provide a meaningful solution  $\hat{\mathbf{x}}$  of the linear system of equations in (1).

<sup>1</sup>A preliminary version of this work appeared in the conference paper [27]. In the present paper, a more detailed derivation of the algorithm is described, performance is also evaluated on computer simulated data, and a much more exhaustive validation on real acquisitions is presented. Results are discussed here in much more detail.

In a Bayesian setting, all quantities are treated as single realizations of random processes, to which a suitable pdf  $p(\cdot)$  is assigned [31]–[33]. In this context, the two most common estimation paradigms are maximum likelihood (ML) and MAP, respectively seeking the realization of  $\mathbf{x}$  maximizing the log-likelihood  $\ln[p(\mathbf{y}|\mathbf{x})]$  and the log-posterior  $\ln[p(\mathbf{x}|\mathbf{y})]$  [34].

In the case of white Gaussian measurement noise  $\mathbf{n}$ , the ML estimate corresponds to the least squares solution  $\hat{\mathbf{x}}_{\text{ML}} = \mathbf{H}^\dagger \mathbf{y}$ , where  $\mathbf{H}^\dagger = (\mathbf{H}^T \mathbf{H})^{-1} \mathbf{H}^T$  denotes the Moore-Penrose pseudo-inverse. The ill-conditioning of  $\mathbf{H}$ , an immediate consequence of the band-limited nature of the PSF, makes the so-obtained solutions highly unsatisfactory, because of the unacceptable amplification of the out-of-band noise components. In this context, the MAP technique provides a way to enforce the estimation problem by including some prior belief about the statistical properties of the solution  $\mathbf{x}$ . Specifically it requires a prior distribution  $p(\mathbf{x})$  to be defined so that, using the Bayes' theorem  $p(\mathbf{x}|\mathbf{y}) \propto p(\mathbf{y}|\mathbf{x})p(\mathbf{x})$ , the MAP estimate becomes:

$$\hat{\mathbf{x}}_{\text{MAP}} = \underset{\mathbf{x}}{\operatorname{argmin}} \left\{ \frac{1}{2\sigma_n^2} \|\mathbf{y} - \mathbf{H}\mathbf{x}\|_2^2 - \log p(\mathbf{x}) \right\}, \quad (2)$$

where  $\sigma_n^2$  is the noise variance. The form of  $p(\mathbf{x})$  defines the expression of the constraint in (2) and has a direct impact on the aspect of the obtained solution. In this context, the common approach is to adopt the prior distribution  $p(\mathbf{x})$  which makes the deconvolved image meet some visual quality requirement at a reasonable computational expense. This concept will be made clearer in the following, where the two most common prior models, i.e., Gaussian and Laplacian, are presented.

### B. Standard Reflectivity Models

1) *Gaussian Model*: The choice of a multivariate Gaussian model for the tissue response has been widely exploited in deconvolution literature. By substituting  $p(\mathbf{x}) \propto \exp(-(1/2) \cdot \mathbf{x}^T \Sigma_{\mathbf{x}}^{-1} \mathbf{x})$  in (2), the MAP estimation problem results in the (weighted)  $\ell^2$ -norm constrained optimization task:

$$\hat{\mathbf{x}} = \underset{\mathbf{x}}{\operatorname{argmin}} \left\{ \frac{1}{2\sigma_n^2} \|\mathbf{y} - \mathbf{H}\mathbf{x}\|_2^2 + \frac{1}{2} \mathbf{x}^T \Sigma_{\mathbf{x}}^{-1} \mathbf{x} \right\}, \quad (3)$$

which is solved by

$$\hat{\mathbf{x}} = (\mathbf{H}^T \mathbf{H} + \sigma_n^2 \Sigma_{\mathbf{x}}^{-1})^{-1} \mathbf{H}^T \mathbf{y} = \mathbf{W} \mathbf{y}, \quad (4)$$

where  $\mathbf{W}$  is the well-known Wiener filter [30, ch. 8]. The autocorrelation matrix  $\Sigma_{\mathbf{x}}$  of the model has been used in [33] to account for the variations in the echogenicity profile that can be expected in real tissues. Nevertheless, the white approximation  $\Sigma_{\mathbf{x}} = \sigma_x^2 \mathbf{I}$  is often preferred in literature [22], [23], [35]. It physically corresponds to a spatially uniform echogenicity profile. Although this simplified

model allows avoidance of some computational issues connected with the estimation of  $\Sigma_{\mathbf{x}}$  and its inversion, it has been observed to produce appreciable image enhancements.

Despite the advantage of an analytical solution, the Wiener filter causes an undesired over-smoothing of the peaks of signal components associated with the presence of isolated scattering centers [24]. This limits the resolution of deconvolved data. To overcome this effect, a Laplacian prior model may be preferred.

2) *Laplacian Model*: A Laplacian pdf possesses heavier tails than the Gaussian and, hence, there is a greater tolerance for a few occasional large-amplitude samples to occur. For this reason, such a model better represents more realistic tissues with diffusive scatterers superimposed with sparse specular reflectors [24], [25]. If  $\mathbf{x}$  is a collection of independent, identically distributed Laplacian random variables  $x_i$ , the  $\ell^1$ -norm constrained optimization problem is obtained:

$$\hat{\mathbf{x}} = \underset{\mathbf{x}}{\operatorname{argmin}} \left\{ \frac{1}{2\sigma_n^2} \|\mathbf{y} - \mathbf{H}\mathbf{x}\|_2^2 + \lambda \|\mathbf{x}\|_1 \right\}, \quad (5)$$

where  $\lambda = \sqrt{2}/\sigma_x$ ,  $\sigma_x^2$  is the reflectivity variance, and  $\|\mathbf{x}\|_1 = \sum |x_i|$  denotes the  $\ell^1$ -norm. In terms of image the  $\ell^1$ -norm deconvolution produces a superior gain in resolution and contrast. This is obtained at the expense of an increased computational cost because (5) must be solved with an iterative convex optimization routine.

## III. PROPOSED DECONVOLUTION FRAMEWORK

As previously mentioned, deconvolution techniques have been exclusively employed for visual quality enhancement thus far, whereas a conceptually original use is proposed here. The goal is indeed to restore higher quality information on the tissue, to be exploited for its characterization. This requires the deconvolved image to be the most accurate estimate of the tissue reflectivity available.

Wiener and  $\ell^1$ -norm deconvolution are not the most viable candidates in this scenario. Although the statistical models they are based on are sufficient for achieving appreciable visual quality improvements, they are not flexible enough to describe a general tissue response. As a consequence, the use of these techniques implies a bias in the obtained solutions which may distort important structural features that should be preserved in a tissue characterization context. A more flexible model for the tissue reflectivity is needed.

### A. Proposed Model for Tissue Response

We propose to model tissue reflectivity with a generalized Gaussian distribution (GGD) [26]. By suitably adjusting one scale and one shape parameter, this distribution allows sequences of arbitrary energy and sparseness

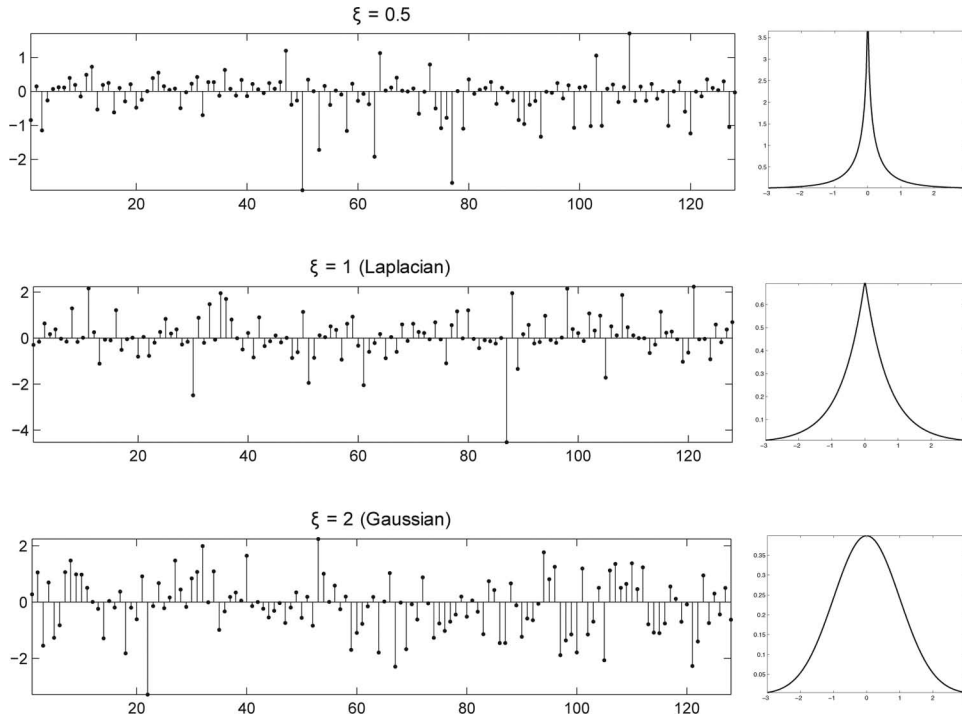


Fig. 1. Examples of random sequences drawn from a zero-mean unit-variance generalized Gaussian distribution, having  $\xi = 0.5$ ,  $\xi = 1$ , and  $\xi = 2$ . To the right of each sequence, the associated probability density is shown. Low values of  $\xi$  nicely model tissues with low concentrations of reflectors. As  $\xi$  increases, higher concentrations are represented.

to be generated (Fig. 1). Because energy is directly connected with the scatterers' average strength and sparseness is intuitively related to their concentration, several kinds of tissues can theoretically be modeled.

The GGD pdf is

$$p(x_i) = a \exp\left(-\frac{|x_i|^\xi}{b}\right), \quad (6)$$

where  $\xi$  is the shape parameter,  $b = \sigma_x \sqrt{\Gamma(1/\xi)/\Gamma(3/\xi)}$  is the scale parameter,  $\sigma_x$  is the standard deviation,  $a = \xi / (2b\Gamma(1/\xi))$  is the normalization term and  $\Gamma(\cdot)$  is the Gamma function. Note that Gaussian and Laplacian distributions are special cases of GGD corresponding to  $\xi = 2$  and  $\xi = 1$ , respectively. Several GGD pdfs corresponding to different shape parameters are illustrated in Fig. 1. The log-posterior function for a GGD prior becomes:

$$L = -\frac{1}{2\sigma_n^2} \|\mathbf{y} - \mathbf{H}\mathbf{x}\|_2^2 - \lambda \|\mathbf{x}\|_\xi^\xi + N \cdot a, \quad (7)$$

where  $\lambda = b^{-\xi}$ ,  $\|\mathbf{x}\|_p = (\sum |x_i|^p)^{1/p}$  denotes the  $\ell^p$ -norm and  $N$  is the total number of samples in the image.

With reference to the general expression (7), classical restoration techniques proceed by *a priori* and arbitrarily fixing  $\xi$  equal to 2 or 1 and then solving the optimization for  $\mathbf{x}$  alone. In the proposed approach, similar assumptions on tissue sparsity will be avoided; this information will be instead restored along with the tissue response. In

this sense, we propose an expectation maximization algorithm for the optimization of (7) with respect to  $(\mathbf{x}, \xi)$ .

### B. Optimization Scheme

The EM algorithm is an iterative procedure for the solution of ML or MAP statistical estimation problems when the solution is not analytically tractable [36]. Each iteration of the EM algorithm consists in an expectation step (E-step), in which the expectation function is defined, and a maximization step (M-step), in which the expectation is maximized to compute the new estimate of the quantity of interest. It can be proved that an EM algorithm monotonically converges to a local maximum of the log-likelihood or log-posterior function.

In [32], an EM framework is derived for the solution of MAP image restoration problems in which the prior  $p(\mathbf{x})$  is expressed as a Gaussian scale mixture (GSM). Because the GGD belongs to this family, that framework can be borrowed here to tackle the deconvolution task at hand. The M-step at iteration  $k$  is given by

$$\text{M-step: } \hat{\mathbf{x}}_{k+1} = (\sigma_n^2 \mathbf{D}_k + \mathbf{H}^T \mathbf{H})^{-1} \mathbf{H}^T \mathbf{y}, \quad (8)$$

where  $\mathbf{D}_k$  is a diagonal matrix of size  $N \times N$  with entries  $[\mathbf{D}]_{ii} = \lambda \xi / |\hat{x}_i^k|^{2-\xi}$ , and  $\hat{x}_i^k$  is the  $i$ th sample of  $\hat{\mathbf{x}}_k$ .

By iterating (8), one guarantees that  $L(\hat{\mathbf{x}}_{k+1}, \xi) > L(\hat{\mathbf{x}}_k, \xi)$ , where  $L$  is defined in (7). Concerning the estimation of  $\xi$  instead, the simplest solution is to add the ML parameter update step after the M-step in (8):

TABLE I. MAP RESTORATION UNDER GENERALIZED GAUSSIAN DISTRIBUTION PRIOR.

---

Initialization:  $\hat{\mathbf{x}}_0 = \mathbf{y}$ ,  $k = 0$   
repeat  
 $\hat{\xi}_k = \operatorname{argmax}_{\xi} L(\hat{\mathbf{x}}_k, \xi)$ ,  
 $d_k^i = \lambda \hat{\xi}_k / |\hat{x}_k^i|^{2-\hat{\xi}_k}$ ,  
 $\mathbf{D}_k = \operatorname{diag}(\mathbf{d}_k)$ ,<sup>1</sup>  $\mathbf{d}_k = [d_k^1, \dots, d_k^N]$ ,  
 $\hat{\mathbf{x}}_{k+1} = (\sigma_n^2 \mathbf{D}_k + \mathbf{H}^T \mathbf{H})^{-1} \mathbf{H} \mathbf{y}$   
 $E = |L(\hat{\mathbf{x}}_{k+1}, \hat{\xi}_k) - L(\hat{\mathbf{x}}_k, \hat{\xi}_k)| / |L(\hat{\mathbf{x}}_k, \hat{\xi}_k)|$   
 $k = k + 1$   
until:  $E < \tau$

---

<sup>1</sup> $\operatorname{diag}(\mathbf{a})$  is the diagonal matrix with vector  $\mathbf{a}$  as entries.

$$\hat{\xi}_{k+1} = \operatorname{argmax}_{\xi} \{L(\hat{\mathbf{x}}_{k+1}, \xi)\}. \quad (9)$$

Such an estimate can be computed in few iterations of the Newton-Raphson scheme proposed in [37].

The complete algorithm is summarized in Table I, where  $\tau$  is an *a priori* fixed threshold value. It should be noted that, because of the ML parameter estimation step in (9), the global framework is no longer rigorously an EM algorithm and therefore convergence is not theoretically guaranteed. Nevertheless, (9) ensures that  $L(\mathbf{x}, \hat{\xi}_{k+1}) > L(\mathbf{x}, \hat{\xi}_k)$  and the monotonic growth of the log-posterior is preserved. Convergence was observed in all of the experiments.

The most time-consuming step is the signal update step in (8), which is equivalent to solving the system  $\mathbf{A}\mathbf{x} = \mathbf{b}$ , with  $\mathbf{A} = (\sigma_n^2 \mathbf{D}_k + \mathbf{H}^T \mathbf{H})$  and  $\mathbf{b} = \mathbf{H}\mathbf{y}$ . Because the direct solution is not computationally feasible, an iterative scheme must be adopted; specifically, a preconditioned conjugate gradients algorithm with Jacobi pre-conditioning was used [38]. Additionally, to make (7) differentiable in the origin, a smooth approximation of the  $\ell^1$ -norm is chosen:  $|x| \sim \sqrt{x^2 + \varepsilon}$ , where  $\varepsilon \ll 1$  [25]. Because the entity of the approximation is dependent on the variance of the signal, we take  $\varepsilon = \gamma \sigma_x^2$ , where  $\gamma$  is a small, positive proportionality constant.

In the remainder of this section, other important issues are addressed. In particular, the modifications implied by considering the complex envelope signal are described, together with the adopted techniques for the estimation of the system PSF along with signal and noise variances  $\sigma_x^2$  and  $\sigma_n^2$ .

1) *IQ Signal*: In this work, we do not process the RF signal directly, but after its baseband demodulation. The resulting signal is complex-valued and is referred as in-phase/quadrature (IQ). The linearity of the demodulation process guarantees that all the discussions made up to this point will still hold for the IQ signal as well, provided that  $\mathbf{y}$ ,  $\mathbf{x}$ , and  $\nu$  now denote complex variables and that Hermitian transpose  $(\cdot)^H$  must be used in place of the transpose  $(\cdot)^T$  when requested. We note also that a redefinition of the GGD for complex variables is needed to keep the al-

gorithm of Table I completely unchanged. Its derivation is addressed in Appendix A.

The IQ signal can be downsampled without aliasing problems. First, it allows a reduction of the computational cost [consider that all of these deconvolution algorithms have a complexity of  $\mathcal{O}(n^2)$ ] and second, because the downsampled signal has a wider relative bandwidth [39], it allows a decrease in the condition number of  $\mathbf{H}$  and enforces the stability of its inversion.

2) *PSF Estimation*: Deconvolution of ultrasound images is known to be a blind problem because  $\mathbf{H}$  is *a priori* unknown [21]. The main reason for this is that the PSF changes its shape during the propagation through the medium. This is principally due to the presence of the investigated tissues between the transducer and the target: dispersive attenuation and phase aberrations are the main sources contributing to this variability [40], [41]. These effects are intrinsically problem-dependent and unpredictable, thereby making any prior guess of the PSF shape, deriving from simulations or measurements, necessarily inaccurate.

The most common way to cope with this problem is to first estimate a suitable PSF from the RF image, and then use the resultant estimate to solve the deconvolution problem in a non-blind manner. PSF estimation has been thoroughly explored in the literature. Most successful techniques are represented by the cepstrum-based homomorphic method introduced by Taxt [22], [35] and the generalized homomorphic method later presented by Michailovich [24], [26]. They both rely on the fact that the log-spectra of the PSF and that of the reflectivity function have different attributes: whereas the former is smooth, at least inside the transducer bandwidth, the latter has a noise-like appearance. Then, cepstrum based techniques proceed by truncating the complex cepstrum (i.e., the Fourier transform of the log-spectrum [39]) of the acquired RF signal to obtain a PSF estimate. Because this abrupt cepstrum truncation may introduce aliasing in the resulting estimate [24], generalized homomorphic techniques overcome this effect by exploiting more elaborate signal processing techniques. In particular, the PSF estimation is presented as a de-noising problem, which is solved in [24] with a three-step wavelet thresholding procedure. An outliers shrinkage step is introduced in [24], [26] to make the estimate insensitive to peaky samples possibly occurring when the reflectivity model deviates from the Gaussian model.

To the best of our knowledge, the generalized homomorphic technique in [24] is the most successful; in particular, it is documented to outperform the most popular cepstrum-based approaches. A more detailed discussion and validation of this technique is beyond of the scope of the present work; the interested reader may find an exhaustive description and evaluation in [24] and [26]. An example of estimated PSF is given in Fig. 2.

The aforementioned PSF variation and the beam shaping determined by the focusing imply that a spatially vari-

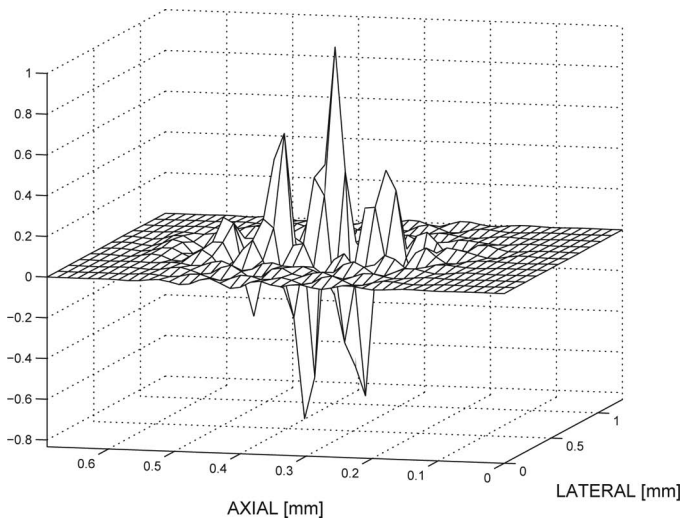


Fig. 2. Point spread function estimated from the phantom data used in the present study. Data were acquired with a 30-MHz transducer and sampled at 500 MHz.

ant blur must be taken into account. An effective solution is to assume a slowly varying PSF and, hence, a PSF that is well approximated by a piecewise constant function so that the image can be divided into several segments formed by a stationary convolution with a different PSF [24], [33]. As shown in [42], a spatially variant PSF can be accounted for by a single blurring matrix  $\mathbf{H}$ . It is built by combining the single PSFs as  $\mathbf{H} = \sum_{k=1}^K D_k \mathbf{H}_k$  ( $K = 4$  in this study), where the matrix  $D_k$  defines the kind of interpolation between the  $k$ th region and the neighboring ones. As shown in [42], a piecewise constant interpolation is computationally efficient (so that the complexity of restoring an image with a spatially variant PSF is comparable to that of spatially invariant restoration).

3) *Estimation of  $\sigma_n$  and  $\sigma_x$* : We adopted the wavelet-based noise variance estimator presented in [33]. It is based on the reasonable assumption that the finest-scale wavelet coefficients  $\mathbf{w}$  of  $\mathbf{y}$  are mainly associated with noise. The estimated noise level is

$$\hat{\sigma}_n = \frac{\text{median}(|\mathbf{w}|)}{\sqrt{\ln 4}}. \quad (10)$$

Assuming unit energy PSFs (this assumption can always be satisfied with a suitable re-scaling) then  $\|\mathbf{H}\mathbf{x}\|_2 \approx \|\mathbf{x}\|_2$  and  $\hat{\sigma}_x^2 \approx \sigma_y^2 - \hat{\sigma}_n^2$ , where  $\sigma_y^2 = \|\mathbf{y}\|_2^2 / (2N)$ .

#### IV. MATERIALS AND METHODS

The ultimate goal of this study was to investigate whether and to what degree the proposed deconvolution framework can affect the characterization of the propagating medium. This was achieved through a validation on experimental data from several tissue-mimicking phantoms having specific scatterer concentrations.

##### A. Experimental Setup

Ultrafine polyamide particles of diameter  $10 \pm 2 \mu\text{m}$  (Orgasol 2001 EXD NAT 1, Arkema Inc., Colombes, France) were used as scatterers. The tissue-mimicking phantoms were prepared by mixing a specific concentration of Orgasol particles with distilled water and 1% w/w ICI Synperonic NP 10 surfactant (Fluka, Sigma-Aldrich Chimie S.a.r.l., St. Quentin Fallavier, France) to improve the particle wetting. Orgasol particles had a density of  $1030 \text{ kg/m}^3$  which supports the weak scattering assumption that is the basis of (1). Seven experiments were performed using 7 mixtures having Orgasol concentrations of 0.25%, 0.5%, 0.75%, 1%, 6%, 12%, and 24%. Low concentrations (0.25% to 6%) constituted random media, whereas higher ones (12% and 24%) mimicked dense media to study more packed distributions of particles, as performed in [43]. A magnetic agitator was employed to ensure that the solution was homogeneous throughout the acquisition. Because the transducer had a focal depth of 12.7 mm, a 6-mm-thick layer of agar gel (Prolabo) at 3% was interposed between the probe and the phantom to place the probe focus in the region of interest. Experiments were carried out at room temperature ( $25^\circ\text{C}$ ). At that temperature, sound velocities in water and agar gel are 1482 [44] and 1540 m/s [45], respectively.

The RF signal was acquired with a high-resolution ultrasound scanner (Vevo 770, Visualsonics Inc., Toronto, Canada), equipped with an RMV-707B single-element transducer (center frequency of 30 MHz). Acquisitions were performed using the ultrasound equipment available at the Animage platform (Cermep, Lyon, France). The RF signal was amplified (pulse/receiver 5052pr, Panametrics, Waltham, MA) and collected at a sampling frequency of 500 MHz with 8-bit resolution (Gagescope, model CS11G8-1, Acquisys, Montigny-le-Bretonneux, France). For each phantom, 3 acquisitions were made. Data was then processed using MATLAB (R2008b, The MathWorks, Natick, MA). The experimental setup is shown in Fig. 3.

Each image was demodulated, downsampled by a factor 8, and deconvolved using Wiener filtering, Laplacian prior, and generalized Gaussian prior. Data was then re-modulated and re-sampled to have an image size identical to that of the unprocessed frames. Each image was then subdivided into 48 non-overlapping regions of interest (ROIs) of  $1 \times 3 \text{ mm}$  ( $50 \times 29$  pixels in our setting), equal to three times the extent of an estimated PSF in each direction. Considering the 3 images per concentration, the total number of ROIs related to a single concentration was equal to 144. Data was then processed according to the flowchart in Fig. 4. A description of each block follows.

##### B. Processing Work-Flow

1) *Deconvolution*: Deconvolution was implemented with the EM algorithm in Table I (stopping rule  $\tau = 0.001$ ). In the Laplacian case,  $\xi$  was kept fixed to 1 and the corre-

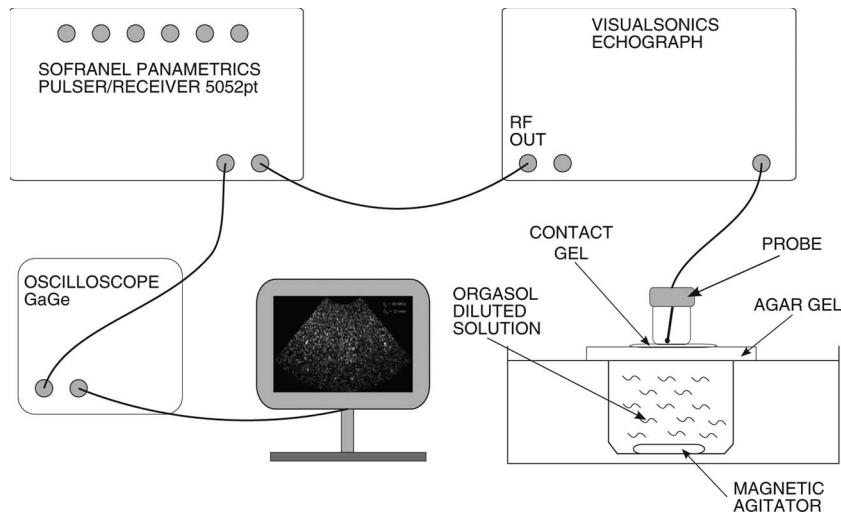


Fig. 3. Experimental setup used in the experiments.

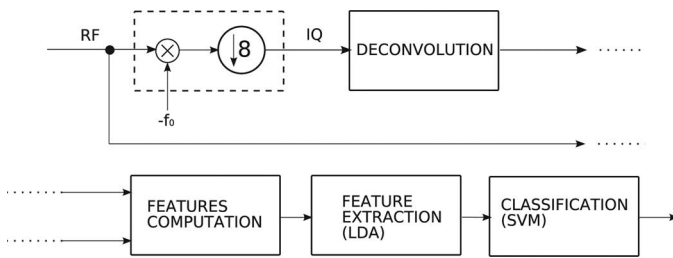


Fig. 4. Processing flowchart.

sponding ML estimation step in (9) was skipped. Roughly 20 iterations were needed for convergence for both the Laplacian and GGD cases. On sub-sampled data ( $210 \times 382$  pixels), each iteration was accomplished in roughly 6 s on a MATLAB implementation (R2010b, The MathWorks) executed on a 2.27-GHz Intel Core i5 (Intel Corp., Santa Clara, CA) laptop equipped with 4 GB of RAM and running Windows 7 64-bit (Microsoft Corp., Redmond, WA). In the Wiener case, the solution is directly obtained by (4), so that the computational time is equal to that of a single iteration of the iterative EM algorithm ( $\sim 6$  s).

2) *Feature Set*: In this study, statistical features were used for the characterization. They are obtained by fitting data amplitude histograms with appropriate parametric pdfs. In particular, a GGD was used to fit the RF signal [20], Nakagami distribution for the envelope [15], and Nakagami for the compressed B-mode as well [18] (for simplicity, we will refer these last two features as Nakagami-envelope and Nakagami-bmode). Each of these three distributions has two parameters, called shape and scale. The total number of features is, therefore, six. Although the scale is fundamentally a measure of the signal energy, the shape parameter is instead directly correlated with scatterer concentration. These features seem, therefore, highly appropriate in relation to the described setup.

3) *Feature Extraction*: As mentioned, the six adopted features are basically associated with two physical properties: echogenicity and density. Although exploiting different data representations (i.e., RF, uncompressed envelope, and B-mode) may bring a degree of complementarity in the information, this could otherwise produce some correlation between features of the same kind. When similar situations are encountered, it is common to process the entire dataset of the computed features with a feature extraction technique. Feature extraction is a common strategy in pattern recognition, which linearly maps data into a space of lower dimension. This is constructed in such a way that data are still described with a sufficient accuracy in the new space [46]. Feature extraction is meant to improve the accuracy of a classification algorithm by preventing over-fitting and is beneficial in terms of memory consumption and computational burden.

The most standard solution to the problem is represented by the principal component analysis (PCA), in which the axes of the sub-space coincide with the eigenvectors of the data covariance matrix which have the highest eigenvalues. When a training set of labeled data are available, as in our case in which the exact concentrations are known, a better supervised alternative to PCA is represented by linear discriminant analysis (LDA) [46, ch. 4]. This further knowledge is exploited in the definition of a subspace which maximizes the interclass separation with respect to the intraclass dispersion. In this work we adopted LDA for projecting data into a subspace of dimension equal to 2. We verified that this dimension is sufficient for explaining more than 98% of data variation in all the considered experiments.

To evaluate the effective contribution of feature extraction, all of the experiments were carried out both with and without this step. In all of these cases, the better results were observed when LDA was applied.

4) *Classification*: Both linear and non-linear classification schemes were tested. Nonlinear methods were found

to be largely preferable in terms of classification errors and computation time. In particular, a support vector machine (SVM) with radial basis functions as kernels was used [46, ch. 5]. Kernel variance was selected by cross validation as detailed in Section V.

Feature extraction and classification part was performed with the statistical pattern recognition toolbox developed for Matlab [47].

Note that the main scope of this work is expressively to evaluate the deconvolution effect inside a classification task and not to provide a standard flow for ultrasonic tissue characterization. For this reason, the classification scheme summarized here may be suboptimal, but is otherwise sufficient to give trustworthy insights into the effects of a deconvolution step.

## V. RESULTS

The algorithm performance was evaluated on computer simulations and on the phantom studies described previously.

### A. Computer Simulations

The synthetic reflectivity was implemented as a numerical matrix with the same size as the acquired echo phantom images. Reflectivity samples were modeled as a collection of randomly placed scatterers that have a scattering strength with a Gaussian distribution (the same

model employed inside the Field II software [48]). The number of scatterers was set to reproduce the same concentrations used in the Orgasol phantoms acquisitions. A background of 10-dB-weaker scatterers was added to mimic the diffusive signal component. Their amplitude followed a Gaussian distribution and they were placed to fill every entry left empty in the numerical matrix implementing the tissue reflectivity. The synthetic RF image was then obtained by convolving the synthetic reflectivity with a spatially variant PSF, obtained from one of the acquired Orgasol phantoms by means of the generalized homomorphic technique described in Section III-B. Gaussian noise was added for a signal to noise ratio of 20 dB. Simulated RF images were then deconvolved with the three techniques under consideration. No prior knowledge of the PSF was assumed when deconvolution was performed. Features were computed on simulated and deconvolved data as described in Section IV-B.

By making a synthetic reflectivity available, computer simulations allow to better discussion of two key elements at the basis of the proposed framework: 1) the ideal reflectivity would be easier to classify than the measured signal; and 2) the presented algorithm manages to restore closer reflectivity estimates compared with the considered Wiener and  $\ell^1$ -norm deconvolution.

A proof of the first point is provided by Fig. 5. It illustrates the clusters relative to simulated 0.25% and 0.75%

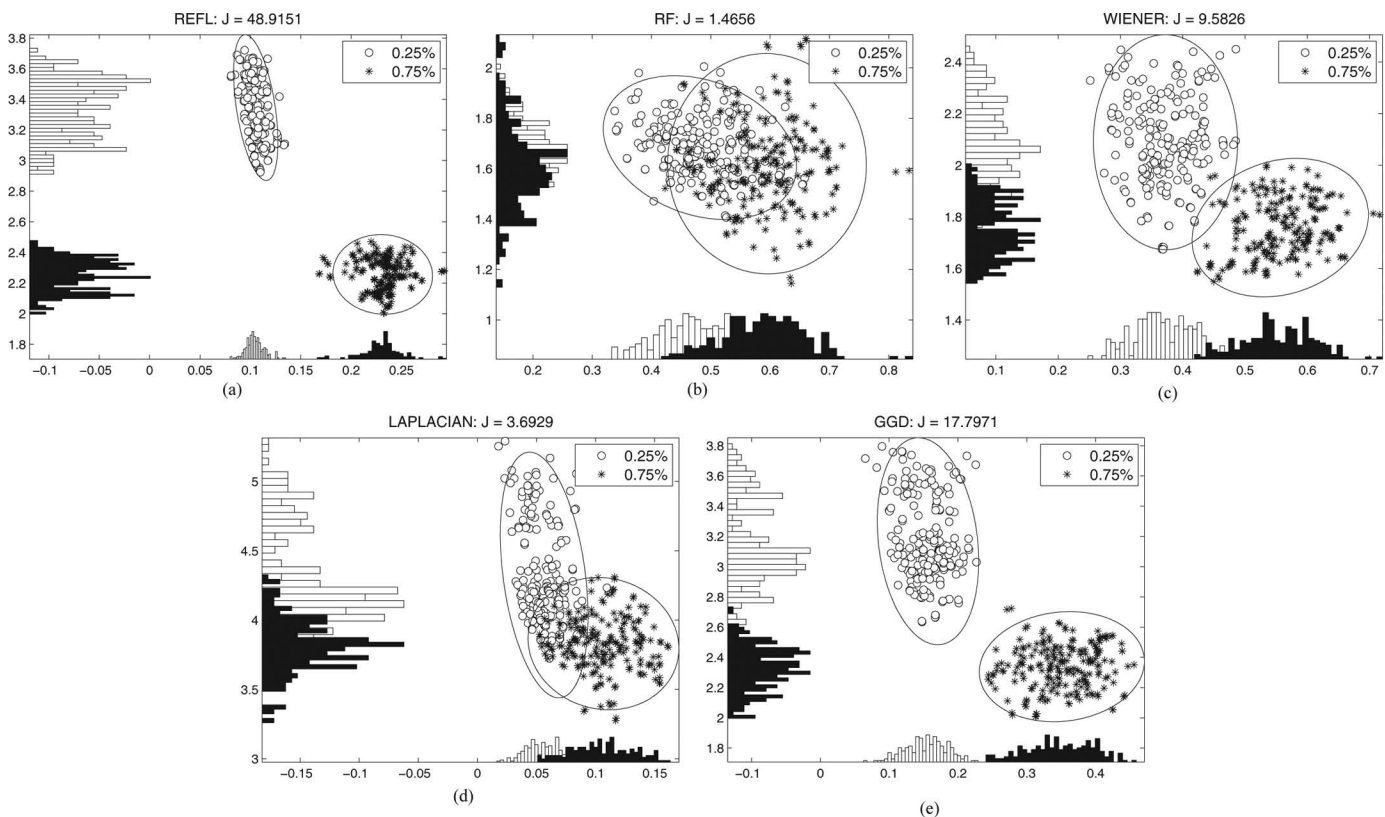


Fig. 5. Feature space corresponding to the generalized Gaussian distribution shape parameter ( $x$ -axis) and Nakagami shape parameter for the envelope signal ( $y$ -axis) for different kinds of data representations: (a) tissue reflectivity (REFL), (b) RF signal, (c) after Wiener filtering, (d) after  $\ell^1$ -norm deconvolution, (e) after the proposed algorithm (GGD). Confidence ellipses at 80% are displayed as well. The Mahalanobis distance  $J$  between the two clusters is reported on each subfigure.



TABLE II. SEPARATION WITH REFLECTIVITY CLUSTER.

Concentration	Original	Laplacian	Wiener	GGD
0.25%	116.47	2.31	59.99	0.31
0.5%	40.38	2.09	20.76	0.39
0.75%	122.29	9.82	67.66	0.20
1%	103.29	5.88	85.85	2.94
6%	76.51	13.96	53.75	1.61
12%	40.67	30.95	48.40	4.65
24%	24.13	116.54	29.28	9.51
$\Sigma$	523.73	181.55	362.69	19.61

concentrations in the 2-D feature space defined by GGD ( $x$ -axis) and Nakagami-envelope ( $y$ -axis) shape parameters. A 2-D projection of the entire 6-D feature space has been used for visualization purposes. These particular features were selected because they are the most relevant for evaluating scatterers' concentration. Let us consider Figs. 5(a) and 5(b); they represent the clusters position when features are computed on the ideal reflectivity and on the simulated acquired signal respectively. These plots provide a visualization of a concept previously mentioned in this paper, i.e., that an accurate estimation of scatterers concentration is harder to achieve when the RF signal is considered. This is due to the filtering effect associated with the system PSF which determines a mixing of the single scatterers' responses. This effect is not present when the ideal reflectivity is considered [cf. Fig. 5(a)] and this results in a better intercluster separation. Therefore, for an improved characterization of the propagating medium, it would be interesting to restore an approximation of the feature space configuration relative to the ideal reflectivity. This is exactly the goal we want to achieve through deconvolution.

An insight into the capabilities of the three considered deconvolution algorithms to reach this goal is provided by Figs. 5(c)–5(e). As expected, the proposed algorithm is the most appropriate to restore an intercluster separation closer to that of the tissue response. As a measure of the intercluster separation, the Mahalanobis distance is reported at the top of each figure.

A more quantitative evaluation of each algorithm performance is provided in Table II. Each entry reports the Mahalanobis distance<sup>2</sup> [46] between two clusters: the one corresponding to concentration/data-type couple specified by the row/column coordinates and the one relative to the same concentration but obtained from the synthetic reflectivity. Namely, if  $X_c^s$  is the matrix containing the coordinates in the 6-D feature space of the ROIs relative to concentration  $c$  and signal type  $s$  (specifically  $s = \{\text{reflectivity, original, Wiener, Laplacian, GGD}\}$ ), then Table II reports values for  $J(X_c^s, X_c^{\text{reflectivity}})$ , where  $c$  and  $s$  are spec-

ified by the row and column labels respectively. Note that, in this context, the best-performing algorithm is the one producing the smallest values of Mahalanobis distance, because it signifies that a good recovery of the cluster position in the reflectivity feature space has been achieved. The sum of all of the distances for each algorithm is reported in the last table row. This quantity can be interpreted as a measure of the global correspondence between the reflectivity feature space and the one restored after deconvolution. These results show that the proposed algorithm is the one retrieving the most statistically close reflectivity estimates. At the same time, they emphasize the biasing effect associated with the other popular techniques, which is at the origin of the high-distance values. This biasing is particularly evident for the Wiener filter case, and is probably connected to the over-smoothing effect resulting from such a technique.

### B. Phantom Studies

Because computer simulations offer a deeper understanding of the properties of the different algorithms, it is crucial to investigate their behavior on real experimental data. In this sense, phantom acquisitions, by making a ground-truth available, are the best-suited for a trustworthy performance evaluation. Phantom acquisitions were realized as described in Section IV.

1) *Data Classification*: A first set of trials consisted in evaluating the deconvolution effect for data classification, as represented in Fig. 4. Four data sets were separately considered: unprocessed images, Wiener filtered data, data after  $\ell^1$ -norm deconvolution, and after deconvolution with the proposed scheme. Each set was separately classified and the classification error was measured. LDA and SVM were trained with 50% of the ROIs, randomly picked from the entire data set. The remaining 50% was adopted as testing set. For each experiment, cross-validation was used to find the optimal kernel parameters for the SVM. To avoid biasing in the results resulting from the specific choice of training and testing sets, 50 independent trials were run for each experiment.

Because the likelihood of superpositions among clusters increases with their number, classification becomes more challenging when multiple classes are considered. To study the evolution of the algorithm performance in relation with the problem complexity, we analyzed different situations: we started from the simplest binary classifica-

<sup>2</sup>Given two clusters of  $N$  points in an  $M$ -dimensional space represented as  $M \times N$  matrices  $X_1$  and  $X_2$ , the Mahalanobis distance is  $J(X_1, X_2) = (\mathbf{m}_1 - \mathbf{m}_2)^T (\mathbf{S}_1 + \mathbf{S}_2)^{-1} (\mathbf{m}_1 - \mathbf{m}_2)$  where  $\mathbf{m}_i = X_i \mathbf{1}_N / N$  and  $\mathbf{S}_i = X_i X_i^T / N$  ( $i \in \{1, 2\}$ ).  $\mathbf{1}_N$  denotes the column vector with  $N$  elements equal to 1. Batthacharyya distance and Kullback-Leibler divergence were also considered as distance measures and the adoption of these alternative metrics led to qualitatively analogous results.

TABLE III. CLASSIFICATION ERROR ON 50 INDEPENDENT TRIALS (MEAN  $\pm$  STANDARD VARIATION)\*

Classes		Classification Error			
No.	Concentrations	Original	Wiener	Laplacian	GGD
2	[0.5%, 0.75%]	0.07 $\pm$ 0.002	0.06 $\pm$ 0.004	0.02 $\pm$ 0.002	0 $\pm$ 0
3	[0.25%, 6%, 24%]	0.07 $\pm$ 0.004	0.04 $\pm$ 0.002	0.02 $\pm$ 0.003	0.01 $\pm$ 0.001
4	[0.75%, 1%, 6%, 24%]	0.10 $\pm$ 0.004	0.21 $\pm$ 0.009	0.09 $\pm$ 0.004	0.02 $\pm$ 0.003
5	[0.25%, 0.75%, 1%, 12%, 24%]	0.31 $\pm$ 0.005	0.25 $\pm$ 0.004	0.09 $\pm$ 0.004	0.03 $\pm$ 0.003
6	[0.25%, 0.5%, 1%, 6%, 12%, 24%]	0.39 $\pm$ 0.003	0.35 $\pm$ 0.005	0.10 $\pm$ 0.031	0.08 $\pm$ 0.003
7	[0.25%, 0.5%, 0.75%, 1%, 6%, 12%, 24%]	0.42 $\pm$ 0.005	0.39 $\pm$ 0.002	0.18 $\pm$ 0.003	0.16 $\pm$ 0.003

\*Outliers were removed before the computation of the error statistics. They were detected as the values exceeding the distribution mean  $\pm$  three times the standard deviation and were found to affect less than 1% of the measurements in all of the considered situations. A uniform distribution of the errors is considered.

tion case and progressively increased by one the number of classes until the complete 7-class case. The classification error was computed as the number of correctly classified ROIs over their total number. For each case only the ROIs corresponding to the considered concentrations were used in the error computation.

Table III leads to the following considerations:

- Wiener filtering does not significantly improve classification accuracy and it degrades the classification error in the case of 4 classes. This reveals that Wiener filtering, by far the most common restoration technique, is otherwise ineffective in a tissue characterization context. This is probably connected to the associated over-smoothing effect, particularly evident when low concentrations are considered. In these cases, peaky signal components, due to the presence of isolated scatterers, are filtered out and this prevents an effective estimate of their concentration.
- Laplacian prior seems to positively affect the classification performance. This is particularly evident for a high number of classes. This result confirms that the Laplacian pdf is more effective than the Gaussian for providing realistic representations of general reflectivity structures, with the immediate consequence that obtained solutions are more consistent estimates of the tissue reflectivity.
- The proposed deconvolution scheme is found to ensure the best classification performance. A substantial improvement is obtained with respect to unprocessed data or Wiener filtering. The improvement with respect to the Laplacian case is lower but still remains noticeable, in particular a relative error reduction of 66%, 55%, 20%, and 11% can be observed in the 4-, 5-, 6-, and 7-class cases. These numbers become more significant when considering that the increase of computation required by the proposed technique with respect to the Laplacian case is practically negligible, because the shape parameter estimation step in (9) is extremely efficient. As observed in the simulations, the experimental results confirm that the obtained reflectivity estimates have superior capabilities in discriminating tissues compared with traditional techniques.

The results in Table III can be better explained by observing the ROI distribution in the feature space that the classifier must deal with. This representation is provided in Fig. 6, where the two situations before (left) and after (right) deconvolution with the proposed algorithm are compared. As expected from the computer simulations, the proposed technique restores a better separation among clusters. The new feature space can be finely partitioned by the SVM classifier with improved accuracy.

To evaluate how the classifier performance varies as a function of the positioning of the discriminant boundary, we computed several receiver operating characteristic (ROC) curves relative to different binary classification cases. Two examples are given in Fig. 7, where the areas  $A$  under ROC curves are reported as performance indexes. In these cases, the characteristic closer to the ideal one ( $A = 1$ ) is always observed when deconvolution with GGD prior is used. An improvement is also obtained when the  $\ell^1$ -norm technique is used, whereas Wiener filtering is substantially equivalent to the unprocessed case, as was observed in Table III. An exhaustive evaluation on all of the possible class pairs is shown in Fig. 8, in which the proposed technique always assesses the highest values. It is worth noting that in two-class cases, an accurate classification is always attained, as confirmed by the high values of the ROC curves areas. As a consequence, the improvement provided by deconvolution is not as evident as it is for multiple-class cases.

We conclude this section by noting that the results presented on ROC curves can only be interpreted as a qualitative evaluation of the algorithm performance because the number of samples used for the curve computation (72 for each class) may sometimes be insufficient to make the area differences statistically meaningful, especially in the case of very similar values. For example, although in the case of Fig. 7(a), the reported areas are statistically different ( $\alpha = 0.05$ , one-tailed)<sup>3</sup> for all the couples GGD-Laplacian ( $p < 0.006$ ), GGD-Wiener ( $p < 0.0001$ ), and GGD-RF ( $p < 0.0005$ ), this is not the case for the results in Fig. 7(b), where the curves are closer and there are not

<sup>3</sup>Statistical comparison of the areas under the ROC curves was performed with the non-parametric technique of DeLong *et al.* [49]. The developed framework translates into a simple  $z$ -test where the null hypothesis is that the two areas are equal.

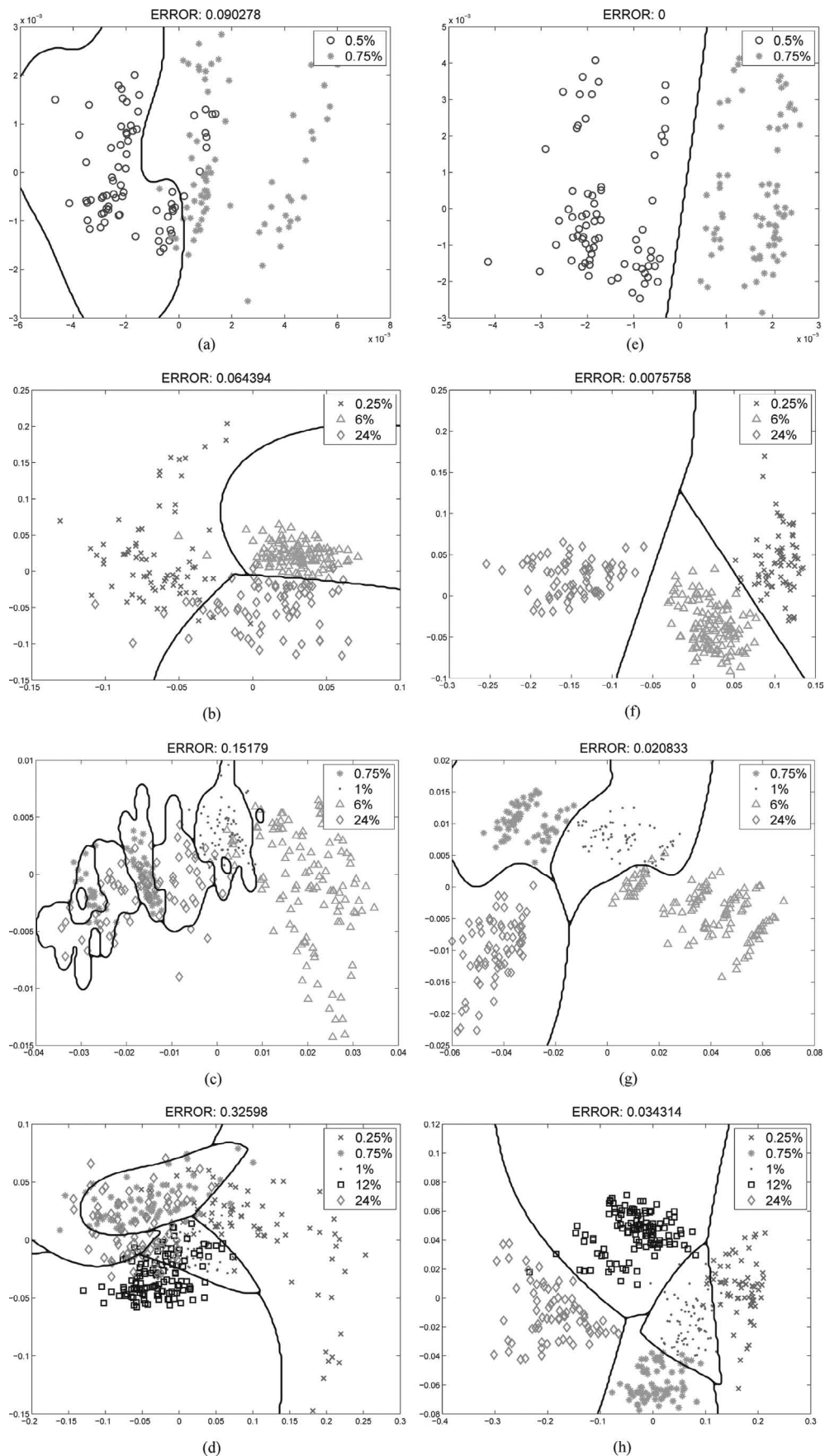


Fig. 6. Scatter plot of the regions of interest in the feature space (testing set only) before [(a)–(d)] and after [(e)–(h)] deconvolution with the proposed technique. The axes correspond to the two features extracted with the linear discriminant analysis. Each row corresponds to a different number of classes. The black lines are the interclass boundaries located by the support vector machine.

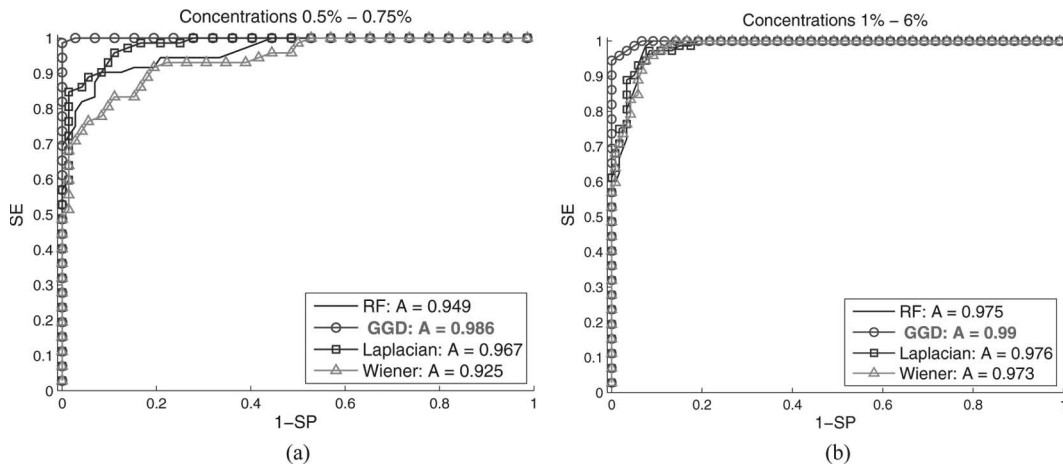


Fig. 7. Receiver operating characteristic curves for two pairs of concentrations.

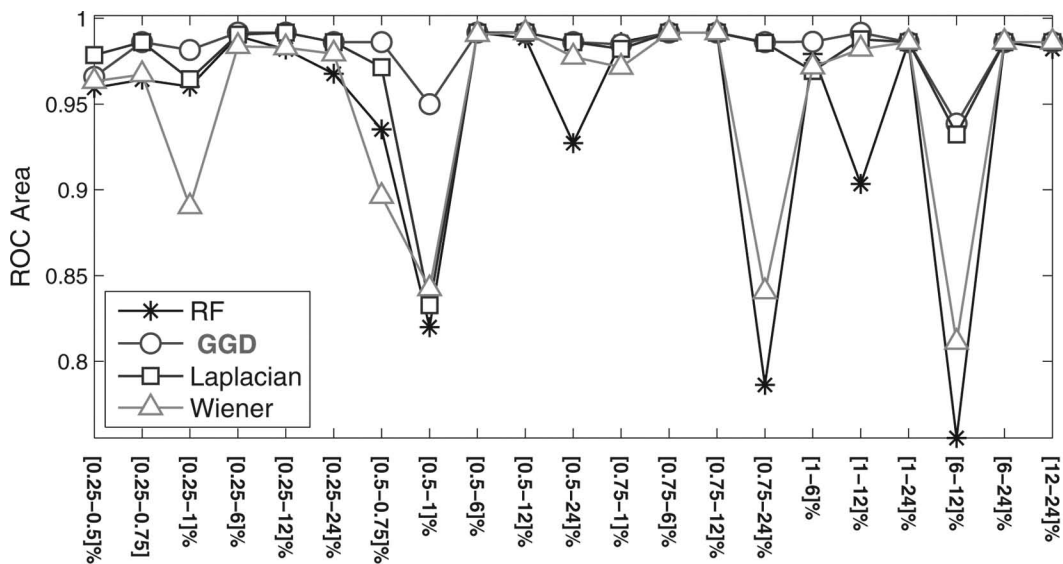


Fig. 8. Area under the receiver operating characteristic (ROC) curve for all concentration pairs.

enough samples to attribute to their distance a statistical consistency. Similar considerations hold also for some of the combinations in Fig. 8.

Although these observations certainly motivate a further validation on a larger set of acquisitions, they do not invalidate what was previously stated about the tendency that these results confirm.

2) *Feature Ranking*: The presented results show that deconvolved data, at least in the considered setting, have a superior characterization capability when the proposed algorithm is used. Because these results derive from considering the entire feature set at one time, it would be interesting to study how each feature contributes to the classification before and after deconvolution.

With that goal, a binary classification task was considered (0.5% and 0.75% concentrations). The 6 considered features were computed on unprocessed and deconvolved data and collected into a 12-elements feature set. Features were then ranked according to their capabil-

ity of separating the two clusters in the feature space. Mahalanobis distance was employed as the intercluster distance metric. The total number of classified samples in this study was 576 (48 ROIs per image, 3 images per concentration, 2 concentrations, unprocessed and deconvolved data). Sequential forward selection (SFS) criterion was used for the ranking [46, ch. 9, p. 315]. SFS is a common bottom-up procedure that adds one feature at a time until the complete set is reached. Specifically, one finds at position  $n$  the feature that, in conjunction with the  $n - 1$  previous ones, determines the maximum inter-cluster distance in the corresponding  $n$ -dimension feature space.

The obtained ranking is reported in Table IV, in which the sorting order is from the first classified to the last. Tags D and U are associated with features computed on data deconvolved with the proposed techniques and unprocessed data, respectively. The fourth column shows the Mahalanobis distance  $J_{1D}$  corresponding to the single-attribute feature set.

TABLE IV. FEATURES RANKING.

Type	Feature name	Signal	$J_{ID}$
D	GGD* shape	RF	3.50
D	Nakagami scale	B-mode	1.62
D	Nakagami shape	B-mode	1.26
U	Nakagami scale	B-mode	0.27
D	Nakagami scale	Envelope	0.95
U	Nakagami scale	Envelope	0.42
U	Nakagami shape	Envelope	0.18
D	GGD scale	RF	0.73
U	GGD scale	RF	0.41
U	Nakagami shape	B-mode	0.44
U	GGD shape	RF	0.28
D	Nakagami shape	Envelope	0.70

\*GGD = generalized Gaussian distribution.

Several observations can be made:

- The first positions in the ranking were occupied by features computed on deconvolved data. This further proves that better-characterizing information on the insonified medium can be restored after deconvolution.
- If sorted by  $J_{ID}$ , all D-tagged features occupy higher positions than U-tagged ones. That is to say, each feature improves its individual discrimination capability when computed on deconvolved data.
- The GGD shape parameter placed first in the ranking. We remark that this is the same value assumed by  $\xi$  at convergence of the algorithm in Table I. This result demonstrates that the proposed deconvolution framework not only produces reflectivity estimates which can be exploited for a better characterization, but gives as a direct output a feature which is, itself, extremely relevant for tissue typing. An illustration of this is given in Fig. 9, where the GGD shape parameter distribution for 4 concentrations is compared for different kind of processing. From the figure the superiority of this parameter when used in conjunction with the proposed deconvolution algorithm is evident. We observe as well that Fig. 9(d) highlights a clear correlation between scatterer concentration and shape parameter. This last effect deserves more consideration in further studies because it could be exploited in interesting applications as for ultrasound-based particle concentration sensing.

Because the ranking results clearly depend on the choice of the two classes, we carried out the same experiments for different couples. In all of those cases, the first-ranked feature was the D-tagged GGD shape parameter (as could have been anticipated from the observation of Fig. 9) and in general the first positions in the ranking were systematically occupied by features deriving from deconvolved images, which proves the generality of the considerations made in this section.

## VI. DISCUSSION AND CONCLUSIONS

In this paper, we have studied the possibility of improving ultrasonic tissue characterization by means of a deconvolution pre-processing step. In this sense, the limitations of the state-of-the-art Wiener and  $\ell^1$ -norm deconvolution techniques have been theoretically analyzed and experimentally confirmed. These limitations principally reside in the choice of simplified models for the reflectivity prior distribution. Although these are sufficient for providing image visual quality improvements, as the deconvolution algorithms are usually used to provide, they are otherwise ineffective for providing statistically close representations of the tissue reflectivity. In this context, an original deconvolution technique has been presented which, because of a more flexible model for the tissue response, manages to overcome the limitations associated with standard solutions. Deconvolution is tackled as a maximum *a posteriori* restoration problem, iteratively solved with an EM procedure.

The algorithm performance was assessed both on numerical simulations and experimental acquisitions. From the former, we were able to better illustrate the properties of the considered deconvolution techniques. In particular, it was observed that the statistically closest reflectivity estimates were obtained when the proposed technique was adopted.

An evaluation on experimental data was then presented based on acquisitions of tissue-mimicking phantoms. From these studies, we were able to make several considerations concerning the employment of standard deconvolution routines. In particular, it was observed that the widely adopted Wiener filtering is not a suitable choice when dealing with tissue classification. However, the employment of  $\ell^1$ -norm seems to be relatively beneficial. We also verified that the proposed deconvolution scheme allowed classification of our data set with the highest accuracy. These phantom studies also showed the noticeable significance of the GGD shape parameter (the  $\xi$  value at convergence) as a feature for tissue typing. In particular, its sensitivity to particle concentration was observed. This aspect would make it extremely interesting to evaluate its usefulness for ultrasound-based concentration measurement applications, e.g., in non-invasive determination of hematocrit [50], [51].

The results obtained encourage, in our opinion, additional studies on data of clinical interest. In this sense, a few considerations must be made. First, the algorithm, as described in this paper, exploits a stationary model of tissue reflectivity; indeed, constant GGD parameters are assumed for the whole image. Such an assumption is well satisfied on the homogeneous phantoms used in the validation, but may be less applicable on images of biological tissues, in which multiple tissues with different acoustical properties are simultaneously imaged. These cases could be accounted for by a nonconstant image map of the shape parameter, to be iteratively updated in the optimization flow. Moreover, complementary stud-

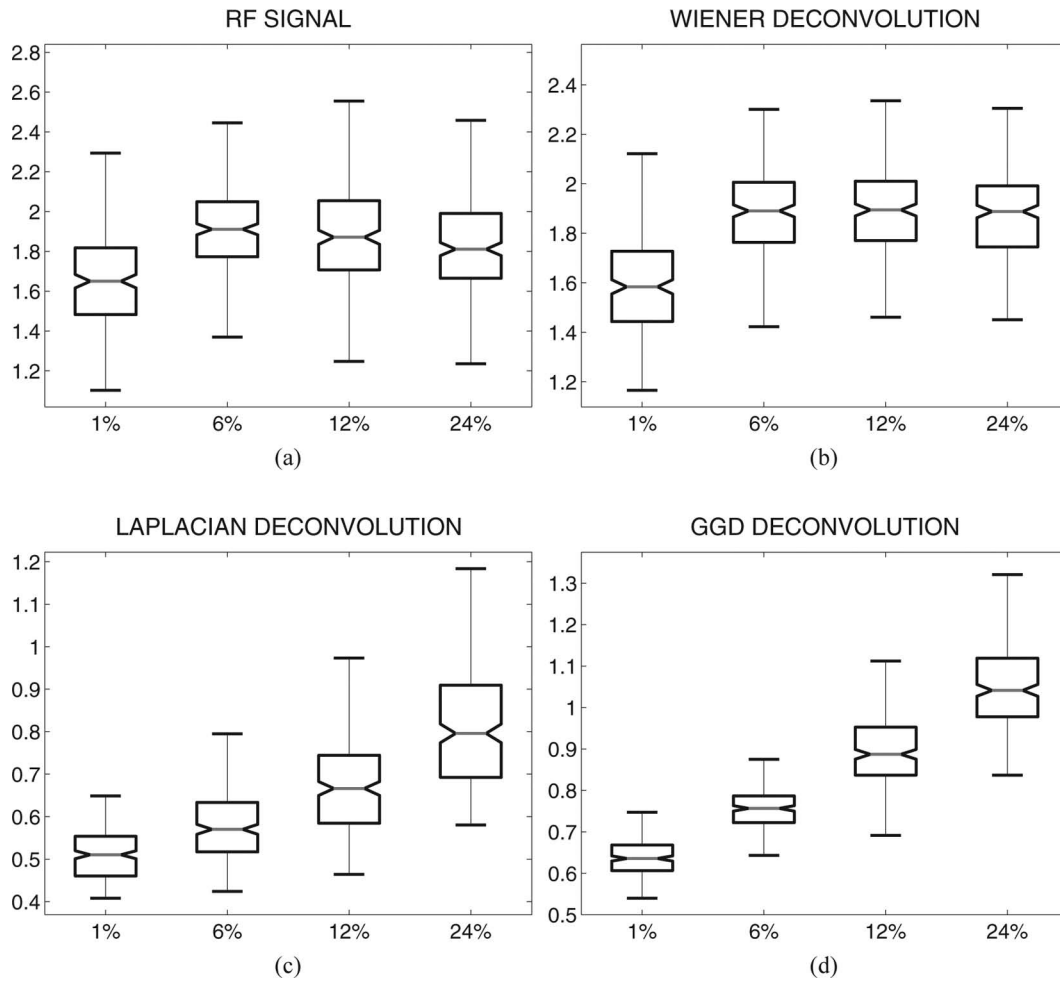


Fig. 9. Generalized Gaussian distribution (GGD) shape parameter box plots for 4 different concentrations.

ies on homogeneous tissue-mimicking phantoms containing polydisperse suspension of scatterers could be done. This will allow the phantoms to better mimic situations of clinical interest, such as cellular size variance during cell death [52], or the simultaneous presence of glandular acini (100  $\mu\text{m}$  diameter) and cell nuclei (14  $\mu\text{m}$  diameter) in breast tumors [53].

A second issue involves the computational complexity. In the current, unoptimized Matlab implementation, every frame is processed in approximately two minutes, which is clearly too slow if assistance during on-line intervention is required. In this context, a substantial increase in speed could be achieved with modern programmable GPU architectures. In particular, the intrinsic parallelism of the algorithm, established by the piecewise constant approximation of the PSF, could be efficiently handled within GPU architectures, for a faster execution.

#### APPENDIX COMPLEX GENERALIZED GAUSSIAN PDF

Consider the complex random variable  $z = x_r + jx_i$ , where both  $x_r$  and  $x_i$  obey a GGD with zero mean, variance  $\sigma^2$ , and shape parameter  $\xi$ . Assuming mutual inde-

pendence of  $x_r$  and  $x_i$ , then  $p(z) = p(x_r)p(x_i)$  [34], where  $p(x_r)$  and  $p(x_i)$  are defined as in (6). Hence,

$$p(z) = a^2 \exp\left(-\left|\frac{x_r}{b}\right|^\xi - \left|\frac{x_i}{b}\right|^\xi\right), \quad (11)$$

and correspondingly  $\ln p(z) \propto (|x_r|^\xi + |x_i|^\xi)$ , which, unless  $\xi = 2$ , is different from  $|z|^\xi$ . This fact prevents the restoration problem to be formalized as an  $\ell^p$ -norm optimization task.

Therefore, to preserve the desired formalism, we define here a variation of the GGD for complex variables, which is written as

$$p(z) = a^2 \exp\left(-\left|\frac{z}{d}\right|^\xi\right), \quad (12)$$

where  $d$  is determined to satisfy the normalization condition  $\iint p(z) dx_i dx_r = 1$ , which leads to

$$d = b \cdot \frac{\sqrt{2/\xi} \cdot \Gamma(2/\xi)}{\sqrt{\Gamma(2/\xi)} \cdot \sqrt{\pi}}. \quad (13)$$

The requested integral can be easily computed by substituting  $z = \rho \exp(j\theta)$ , so that  $dx_r dx_i = \rho d\rho d\theta$ .

## ACKNOWLEDGMENTS

The authors acknowledge the technical assistance of F. Duboeuf and D. Vray on this project.

## REFERENCES

- [1] M. Moradi, P. Mousavi, and P. Abolmaesumi, "Computer-aided diagnosis of prostate cancer with emphasis on ultrasound based approaches: A review," *Ultrasound Med. Biol.*, vol. 33, no. 7, pp. 1010–1028, 2007.
- [2] D. Fukuoka, Y. Ikedo, T. Hara, H. Fujita, E. Takada, T. Endo, and T. Morita, "Development of breast ultrasound CAD system for screening," *Lect. Notes Comput. Sci.*, vol. 4046, pp. 392–398, Sep. 2006.
- [3] J. Thijssen, A. Starke, G. Weijers, A. Haudum, K. Herzog, P. Wohlsein, J. Rehage, and C. De Korte, "Computer-aided B-mode ultrasound diagnosis of hepatic steatosis: A feasibility study," *IEEE Trans. Ultrason. Ferroelectr. Freq. Control*, vol. 55, no. 6, pp. 1343–1354, Jun. 2008.
- [4] F. L. Lizzi, M. Greenebaum, E. J. Feleppa, M. Elbaum, and D. J. Coleman, "Theoretical framework for spectrum analysis in ultrasonic tissue characterization," *J. Acoust. Soc. Am.*, vol. 73, no. 4, pp. 1366–1373, 1983.
- [5] T. Liu, F. L. Lizzi, J. A. Ketterling, R. H. Silverman, and G. J. Kutcher, "Ultrasonic tissue characterization via 2-D spectrum analysis: Theory and in vitro measurements," *Med. Phys.*, vol. 34, no. 3, pp. 1037–1046, Mar. 2007.
- [6] F. L. Lizzi, E. J. Feleppa, S. K. Alam, and C. X. Deng, "Ultrasonic spectrum analysis for tissue evaluation," *Pattern Recognit. Lett.*, vol. 24, no. 4–5, pp. 637–658, 2003.
- [7] O. Basset, Z. Sun, J. Mestas, and G. Gimenez, "Texture analysis of ultrasonic images of the prostate by means of co-occurrence matrices," *Ultrason. Imaging*, vol. 15, no. 3, pp. 218–237, Jul. 1993.
- [8] S. Maggio, A. Palladini, L. De Marchi, M. Alessandrini, N. Speciale, and G. Masetti, "Predictive deconvolution and hybrid feature selection for computer-aided detection of prostate cancer," *IEEE Trans. Med. Imaging*, vol. 29, no. 2, pp. 455–464, Feb. 2010.
- [9] C.-M. Wu, Y.-C. Chen, and K.-S. Hsieh, "Texture features for classification of ultrasonic liver images," *IEEE Trans. Med. Imaging*, vol. 11, no. 2, pp. 141–152, Jun. 1992.
- [10] F. Rakebrandt, D. C. Crawford, D. Havard, D. Coleman, and J. P. Woodcock, "Relationship between ultrasound texture classification images and histology of atherosclerotic plaque," *Ultrasound Med. Biol.*, vol. 26, no. 9, pp. 1393–1402, 2000.
- [11] J. W. Goodman, *Statistical Optics*. New York, NY: Wiley, 2000.
- [12] R. Wagner, S. Smith, J. Sandrik, and H. Lopez, "Statistics of speckle in ultrasound B-scans," *IEEE Trans. Sonics Ultrason.*, vol. 30, no. 3, pp. 156–163, May 1983.
- [13] P. M. Shankar, R. Molthen, V. M. Narayanan, J. M. Reid, V. Genis, F. Forsberg, C. W. Piccoli, A. E. Lindenmayer, and B. B. Goldberg, "Studies on the use of non-Rayleigh statistics for ultrasonic tissue characterization," *Ultrasound Med. Biol.*, vol. 22, no. 7, pp. 873–882, 1996.
- [14] V. Dutt and J. F. Greenleaf, "Ultrasound echo envelope analysis using a homodyned K distribution signal model," *Ultrason. Imaging*, vol. 16, no. 4, pp. 265–287, 1994.
- [15] P. Mohana Shankar, "A general statistical model for ultrasonic backscattering from tissues," *IEEE Trans. Ultrason. Ferroelectr. Freq. Control*, vol. 47, no. 3, pp. 727–736, May 2000.
- [16] P. M. Shankar, V. A. Dumane, C. W. Piccoli, J. M. Reid, F. Forsberg, and B. B. Goldberg, "Classification of breast masses in ultrasonic B-mode images using a compounding technique in the Nakagami distribution domain," *Ultrasound Med. Biol.*, vol. 28, no. 10, pp. 1295–1300, 2002.
- [17] P.-H. Tsui, C.-K. Yeh, Y.-Y. Liao, C.-C. Chang, W.-H. Kuo, K.-J. Chang, and C.-N. Chen, "Ultrasonic Nakagami imaging: A strategy to visualize the scatterer properties of benign and malignant breast tumors," *Ultrasound Med. Biol.*, vol. 36, no. 2, pp. 209–217, 2010.
- [18] P. H. Tsui, C. C. Huang, and S. H. Wang, "Use of Nakagami distribution and logarithmic compression in ultrasonic tissue characterization," *J. Med. Biol. Eng.*, vol. 26, no. 2, pp. 69–73, May 2006.
- [19] O. Bernard, J. D'hooge, and D. Friboulet, "Statistics of the radio-frequency signal based on K distribution with application to echocardiography," *IEEE Trans. Ultrason. Ferroelectr. Freq. Control*, vol. 53, pp. 1689–1694, 2006.
- [20] O. Bernard, B. Touil, J. D'hooge, and D. Friboulet, "Statistical modeling of the radio-frequency signal for partially and fully-developed speckle based on a generalized Gaussian model with application to echocardiography," *IEEE Trans. Ultrason. Ferroelectr. Freq. Control*, vol. 54, no. 10, pp. 2189–2194, Oct. 2007.
- [21] P. Campisi and K. Egiazarian, Eds., *Blind Image Deconvolution: Theory and Applications*, Boca Raton, FL: CRC Press, 2007.
- [22] T. Taxt and R. Jirik, "Superresolution of ultrasound images using the first and second harmonic signal," *IEEE Trans. Ultrason. Ferroelectr. Freq. Control*, vol. 51, no. 2, pp. 163–175, Feb. 2004.
- [23] T. Taxt and G. Frolova, "Noise robust one-dimensional blind deconvolution of medical ultrasound images," *IEEE Trans. Ultrason. Ferroelectr. Freq. Control*, vol. 46, no. 2, pp. 291–299, Mar. 1999.
- [24] O. Michailovich and D. Adam, "A novel approach to the 2-D blind deconvolution problem in medical ultrasound," *IEEE Trans. Med. Imaging*, vol. 24, no. 1, pp. 86–104, Jan. 2005.
- [25] O. Michailovich and A. Tannenbaum, "Blind deconvolution of medical ultrasound images: A parametric inverse filtering approach," *IEEE Trans. Image Process.*, vol. 16, no. 12, pp. 3005–3019, Dec. 2007.
- [26] O. Michailovich and D. Adam, "Robust estimation of ultrasound pulses using outlier-resistant de-noising," *IEEE Trans. Med. Imaging*, vol. 22, no. 3, pp. 368–381, Mar. 2003.
- [27] M. Alessandrini, S. Maggio, J. Pore'e, L. D. Marchi, N. Speciale, E. Franceschini, O. Bernard, and O. Basset, "An expectation maximization framework for an improved tissue characterization using ultrasounds," *Proc. SPIE*, vol. 7968, art. no. 79680E, 2011.
- [28] J. A. Jensen, "A model for the propagation and scattering of ultrasound in tissue," *J. Acoust. Soc. Am.*, vol. 89, no. 1, pp. 182–190, 1991.
- [29] J. Ng, R. Prager, N. Kingsbury, G. Treece, and A. Gee, "Modeling ultrasound imaging as a linear, shift-variant system," *IEEE Trans. Ultrason. Ferroelectr. Freq. Control*, vol. 53, no. 3, pp. 549–563, Mar. 2006.
- [30] H. C. Amdrews and B. R. Hunt, *Digital Image Restoration*. Upper Saddle River, NJ: Prentice Hall, 1977.
- [31] M. Figueiredo and R. Nowak, "An EM algorithm for wavelet-based image restoration," *IEEE Trans. Image Process.*, vol. 12, no. 8, pp. 906–916, Aug. 2003.
- [32] J. Bioucas-Dias, "Bayesian wavelet-based image deconvolution: A GEM algorithm exploiting a class of heavy-tailed priors," *IEEE Trans. Image Process.*, vol. 15, no. 4, pp. 937–951, Apr. 2006.
- [33] J. Ng, R. Prager, N. Kingsbury, G. Treece, and A. Gee, "Wavelet restoration of medical pulse-echo ultrasound images in an EM framework," *IEEE Trans. Ultrason. Ferroelectr. Freq. Control*, vol. 54, no. 3, pp. 550–568, Mar. 2007.
- [34] S. M. Kay, *Fundamentals of Statistical Signal Processing: Estimation Theory* (Signal Processing Series). Upper Saddle River, NJ: Prentice-Hall, 1993.
- [35] T. Taxt and J. Strand, "Two-dimensional noise-robust blind deconvolution of ultrasound images," *IEEE Trans. Ultrason. Ferroelectr. Freq. Control*, vol. 48, no. 4, pp. 861–866, Jul. 2001.
- [36] A. P. Dempster, N. M. Laird, and D. B. Rubin, "Maximum likelihood from incomplete data via the EM algorithm," *J. R. Stat. Soc., B*, vol. 39, no. 1, pp. 1–38, 1977.
- [37] M. Do and M. Vetterli, "Wavelet-based texture retrieval using generalized Gaussian density and Kullback-Leibler distance," *IEEE Trans. Image Process.*, vol. 11, no. 2, pp. 146–158, Feb. 2002.
- [38] J. R. Shewchuk, "An introduction to the conjugate gradient method without the agonizing pain," Carnegie Mellon Univ., Pittsburgh, PA, Tech. Rep., 1994.
- [39] A. V. Oppenheim and W. R. Schaffer, *Discrete Time Signal Processing*. Upper Saddle River, NJ: Prentice Hall, 2009.
- [40] P. Nayarana, J. Ophir, and N. Maklad, "The attenuation of ultrasound in biological fluids," *J. Acoust. Soc. Am.*, vol. 76, no. 1, pp. 1–4, Jul. 1984.
- [41] K. Wear, "The effects of frequency-dependent attenuation and dispersion on sound speed measurements: Applications in human trabecular bone," *IEEE Trans. Ultrason. Ferroelectr. Freq. Control*, vol. 47, no. 1, pp. 265–273, Jan. 2000.
- [42] J. G. Nagy and D. O'Leary, "Fast iterative image restoration with a spatially-varying PSF," Univ. of Maryland at College Park, College Park, MD, Tech. Rep., 1997.

- [43] T. E. Doyle, A. T. Tew, K. H. Warnick, and B. L. Carruth, "Simulation of elastic wave scattering in cells and tissues at the microscopic level," *J. Acoust. Soc. Am.*, vol. 125, no. 3, pp. 1751–1767, 2009.
- [44] F. A. Duck, *Physical Properties of Tissue: A Comprehensive Reference Book*. San Diego, CA: Academic, 1990.
- [45] J. E. Browne, K. V. Ramnarine, A. J. Watson, and P. R. Hoskins, "Assessment of the acoustic properties of common tissue-mimicking test phantoms," *Ultrasound Med. Biol.*, vol. 29, no. 7, pp. 1053–1060, 2003.
- [46] A. R. Webb, *Statistical Pattern Recognition*, 2nd ed. New York, NY: Wiley, 2002.
- [47] V. Franc. (2011, Oct. 5) "Statistical pattern recognition toolbox (stprtool)." [Online]. Available: <http://cmp.felk.cvut.cz/cmp/software/stprtool/>
- [48] J. A. Jensen and N. B. Svendsen, "Calculation of pressure fields from arbitrarily shaped, apodized, and excited ultrasound transducers," *IEEE Trans. Ultrason. Ferroelectr. Freq. Control*, vol. 39, no. 2, pp. 262–267, Mar. 1992.
- [49] E. R. DeLong, D. M. DeLong, and D. L. Clarke-Pearson, "Comparing the areas under two or more correlated receiver operating characteristic curves: A nonparametric approach," *Biometrics*, vol. 44, no. 3, pp. 837–845, Sep. 1988.
- [50] J. W. McMurdy, G. D. Jay, S. Suner, and G. Crawford, "Noninvasive optical, electrical, and acoustic methods of total hemoglobin determination," *Clin. Chem.*, vol. 54, no. 2, pp. 264–272, 2008.
- [51] W. Secomski, A. Nowicki, F. Guidi, P. Tortoli, and P. Lewin, "Non-invasive in vivo measurements of hematocrit," *J. Ultrasound Med.*, vol. 22, no. 4, pp. 375–384, 2003.
- [52] R. M. Vlad, R. K. Saha, N. M. Alajez, S. Ranieri, G. J. Czarnota, and M. C. Kolios, "An increase in cellular size variance contributes to the increase in ultrasound backscatter during cell death," *Ultrasound Med. Biol.*, vol. 36, no. 9, pp. 1546–1558, 2010.
- [53] M. Oelze, W. D. O'Brien Jr., J. Blue, and J. Zachary, "Differentiation and characterization of rat mammary fibroadenomas and 4t1 mouse carcinomas using quantitative ultrasound imaging," *IEEE Trans. Med. Imaging*, vol. 23, no. 6, pp. 764–771, Jun. 2004.



**Martino Alessandrini** received his M.Sc. degree in electronic engineering from the University of Bologna in 2007 and his Ph.D. degree from the Advanced Research Center on Electronics Systems and Information Technologies Ercole de Castro (ARCES) in May 2011. He currently holds a post-doctoral research grant from the Centre de Recherche en Imagerie Médicale (CREATIS), Lyon, France.

His research is principally dedicated to the processing of medical ultrasound images, with a focus on image restoration, registration, segmentation, despeckling, tissue characterization, and motion tracking techniques.



**Simona Maggio** was born in Naples, Italy, in 1984. She received the M.S. degree (summa cum laude) in electrical engineering from the University of Bologna, Italy, in 2007. Since then, she has been part of the Multiresolution Analysis and Simulation group at Department of Electronics, Computer Science, and Systems (DEIS) of the University of Bologna, where she received the Ph.D. degree in May 2011. In 2009, she was a visiting scientist in the Biomedical Imaging Group at Ecole Polytechnique Fédérale de Lausanne (EPFL), Switzerland. Her studies are focused on ultrasound signals and concern tissue characterization, biomedical image segmentation, modeling and classification, feature selection and extraction problems, data mining for diagnostic purposes, and inverse problems for imaging applications.

**Jonathan Porée** was born in Rennes, France, in 1986. He received his B.Sc. degree in electrical engineering from the National Institute of Applied Sciences (INSA) in Rennes, France, in 2009. He received his M.Sc. degree in imaging sciences in 2010 from the National Institute of Applied Sciences in Lyon. He is currently pursuing a Ph.D. degree at the University of Montreal in biomedical science. His current research interests include ultrasound imaging, statistical modeling, and segmentation.



**Luca De Marchi** received the Dr.Eng. and Ph.D. degrees in electronic engineering in 2002 and 2006, respectively, from the University of Bologna. He prepared his master's thesis in digital signal processing and ASICs design at the Technical University of Berlin (TUB). At the end of 2002, he joined the Department of Electronics, Computer Sciences, and Systems (DEIS) at the University of Bologna.

Currently, he is also with the Advanced Research Center for Electronic Systems (ARCES). His research interests are in multiresolution and adaptive signal processing, with particular emphasis on time–frequency analysis for ultrasound signals and numerical applications.

**Nicolò Speciale** was born in Torino, Italy. He received the Ph.D. degree in electronic engineering and computer science from the University of Bologna, Bologna, Italy, working on the modeling of bipolar and MOS devices for smart power applications. In 2002, he became a Research Associate with the Department of Electronics, Computer Sciences, and Systems (DEIS) at the University of Bologna.

His research interests include analysis of electromagnetic interferences on analog integrated circuits, wavelets, and multirate and adaptive signal processing.



**Emilie Franceschini** received her M.S. degree in mechanical engineering from the Ecole Supérieure d'Ingénieurs de Marseille in 2003, and the Ph.D. degree in acoustics from the University of Provence, Marseille, 2006. In 2007, she was a Postdoctoral Fellow at the Laboratory of Biorheology and Medical Ultrasonics, Research Center of the University of Montreal Hospital, Montreal, QC, Canada.

Since October 2008, she has been a Researcher at the French National Centre for Scientific Research (CNRS) in the Laboratory of Mechanics and Acoustics (CNRS-UPR 7051), Marseille. Her current research interests include ultrasound imaging for biomedical applications, inverse problems, and ultrasound characterization of biological tissues at the microscopic level. She is a member of the French Acoustical Society (SFA) and IEEE.



**Olivier Bernard** received the B.S. and Ph.D. degrees in electrical engineering in 2003 and 2006, respectively, from the National Institute for Applied Sciences of Lyon (INSA-Lyon), France. In 2007, he was a Postdoctoral Research Fellow at the Biomedical Imaging Group of the École Polytechnique Fédérale de Lausanne (EPFL), Switzerland.

In 2007, he became associate professor at INSA-Lyon and a member of the CREATIS laboratory (CNRS 5220, INSERM U1044). In 2008, he obtained the special mention (2nd prize) for best Ph.D. in France awarded by the IEEE Engineering in Medicine and Biology Society. His current research interests include medical image processing. He has a strong interest in image segmentation, statistical modeling, and sampling theories.





**Olivier Basset** was born in Bourg en Bresse, France, in 1963. He received, in 1986, the M.S. degree in biomedical engineering from the National Institute of Applied Sciences of Lyon and University Lyon I, France. He received the Ph.D. degree in signal and image processing in acoustics from the National Institute of Applied Sciences in Lyon, in 1991. He is currently a Professor in the University Claude Bernard-Lyon I.

He is a member of the CREATIS Laboratory (CNRS 5220, INSERM U1044). His research interests concern ultrasonic image processing: elastography, tissue characterization, and nonlinear imaging.